JACS
JOURNAL OF THE AMERICAN CHEMICAL SOCIETY
pubs.acs.org/JACS
Article

Enhancement of van der Waals Interlayer Coupling through Polar Janus MoSSe

Kunyan Zhang,[#] Yunfan Guo,*[,#] Qingqing Ji,[#] Ang-Yu Lu, Cong Su, Hua Wang, Alexander A. Puretzky, David B. Geohegan, Xiaofeng Qian, Shiang Fang, Efthimios Kaxiras, Jing Kong,* and Shengxi Huang*

Cite This: J. Am. Chem. Soc. 2020, 142, 17499−17507
Read Online
ACCESS | Metrics & More | Article Recommendations | Supporting Information

ABSTRACT: Interlayer coupling plays essential roles in the quantum transport, polaritonic, and electrochemical properties of stacked van der Waals (vdW) materials. In this work, we report the unconventional interlayer coupling in vdW heterostructures (HSs) by utilizing an emerging 2D material, Janus transition metal dichalcogenides (TMDs). In contrast to conventional TMDs, monolayer Janus TMDs have two different chalcogen layers sandwiching the transition metal and thus exhibit broken mirror symmetry and an intrinsic vertical dipole moment. Such a broken symmetry is found to strongly enhance the vdW interlayer coupling by as much as 13.2% when forming $MoSSe/MoS_2$ HS as compared to the pristine MoS_2 counterparts. Our noncontact ultralow-frequency Raman probe, linear chain model, and density functional theory calculations confirm the enhancement and reveal the origins as charge redistribution in Janus MoSSe and reduced interlayer distance. Our results uncover the potential of tuning interlayer coupling strength through Janus heterostacking.

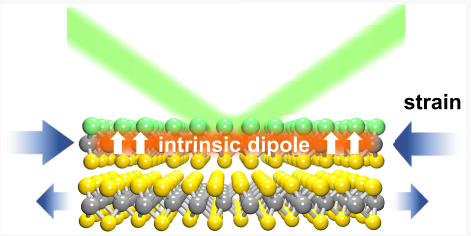

Downloaded via PENNSYLVANIA STATE UNIV on May 27, 2021 at 09:25:25 (UTC).
See https://pubs.acs.org/sharingguidelines for options on how to legitimately share published articles.

INTRODUCTION

The unraveled potential of stacking and twisting van der Waals (vdW) materials to generate unconventional quantum phenomena, such as Mott insulating,[1,2] superconductivity,[3,4] and topological polaritons,[5] has been witnessed in recent years. In stacked two-dimensional (2D) layers, interlayer coupling modified by the twisting angle or the external electric field governs their transport and photonic properties.[6−9] Thus, controlling and even enhancing the interlayer vdW coupling can significantly push fundamental understanding and benefit device applications of 2D heterostructures (HSs). Recently, a new type of 2D materials termed Janus transition metal dichalcogenide (TMD) has been theoretically proposed[10−12] and experimentally realized by selenization or sulfurization through chemical vapor deposition (CVD)[13,14] or low-energy implantation from pulsed laser deposition (PLD) plasma.[15] In contrast to conventional TMDs, the chalcogens on one side of Janus TMD are different from those on the other side (Figure 1a). It follows that monolayer Janus TMDs have broken mirror symmetry to the basal plane and an intrinsic out-of-plane dipole moment due to the electronegativity difference between the chalcogens.[16] Intuitively, the reduced symmetry of polar Janus TMDs leads to unconventional optical and electronic properties absent in conventional TMDs. For instance, it has been experimentally demonstrated that the lack of mirror symmetry in monolayer MoSSe is responsible for out-of-plane piezoelectricity,[13] incident angle-dependent second harmonic generation,[13] and surface-enhanced Raman scattering of biomolecules.[17] Furthermore, the intrinsic dipole moment in Janus TMDs theoretically contributes to effective charge separation,[18] extra-long exciton lifetime,[19] remarkable photocatalytic water-splitting,[20,21] and giant Rashba splitting.[22]

For Janus TMD related HSs, the intrinsic dipole moment is expected to play a key role in the interlayer coupling by functioning as a built-in electric field, a technique widely used to tune the interlayer coupling in vdW HSs,[23] as well as to modulate the valley degree of freedom in nonpolar TMDs.[24,25] To probe the interlayer coupling in Janus TMD related HSs, low-frequency (LF) Raman spectroscopy offers a vibrational-frequency detection limit down to several cm^{-1} (<1 meV). Originating from the relative vibrations between layers, LF modes are fingerprints of both thickness and stacking configuration for a wide range of 2D materials, such as MoS_2,[26−29] WSe_2,[30] and black phosphorus.[31,32] Hence, the LF modes of Janus TMDs and Janus TMD related HSs are promising to signify the strain- and dipole-modulated interfacial properties. Despite the great theoretical efforts,[10−12,18−22] there have been very few experimental investigations into the optical properties of vdW HSs involving Janus TMDs.

Here, we focus on probing the interlayer coupling of $MoSSe/MoS_2$ HSs (i.e., Janus HSs) by LF Raman spectroscopy. For the first time, Janus HSs were directly converted

Received: June 30, 2020
Published: September 17, 2020

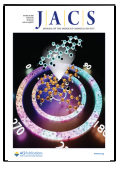

© 2020 American Chemical Society

https://dx.doi.org/10.1021/jacs.0c07051
J. Am. Chem. Soc. 2020, 142, 17499−17507

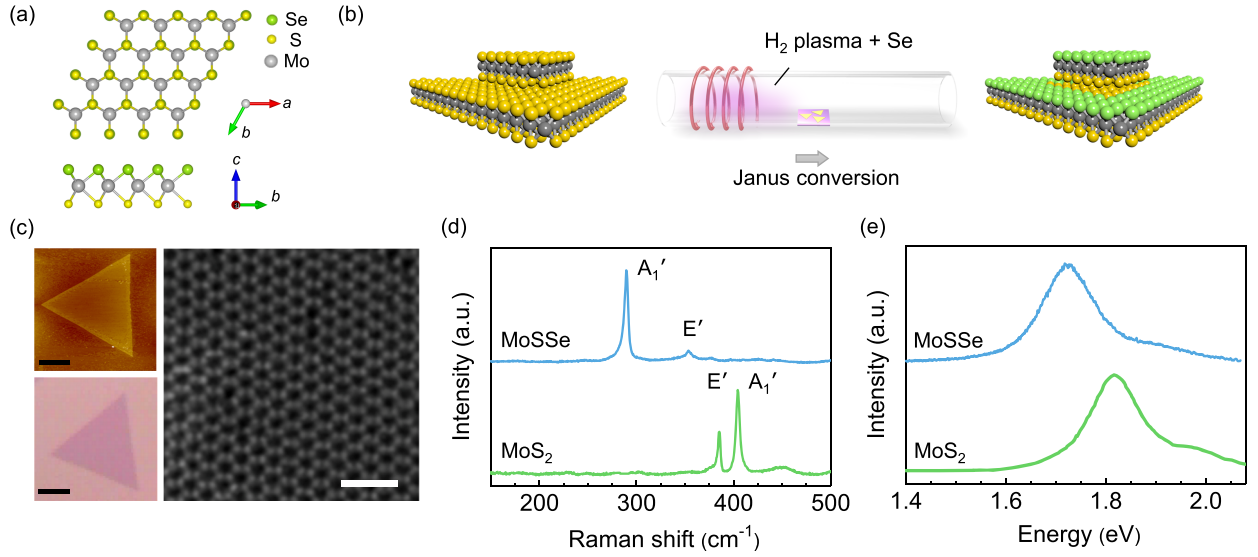

Figure 1. Synthesis and characterizations of Janus MoSSe. (a) Crystal structure of MoSSe monolayer: bottom view (up) and side view (down). (b) Schematics of the synthesis procedure of Janus MoSSe and MoSSe/MoS_2 HSs. (c) Atomic force microscopy (AFM, top left), optical microscopy (OM, bottom left), and MAADF-STEM images (right) of monolayer MoSSe. Scale bars: 2 μm for AFM and OM, 1 nm for MAADF-STEM. (d) Raman and (e) PL spectra of CVD-synthesized MoS_2 and Janus MoSSe show differences in lattice vibrations and photoemissions.

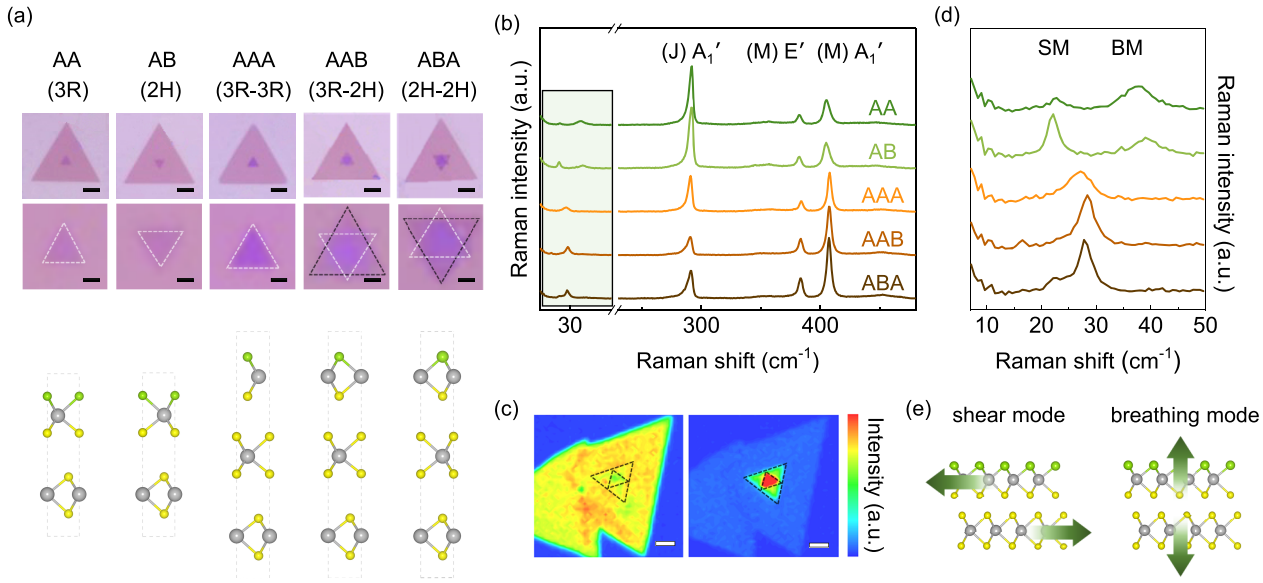

Figure 2. MoSSe/MoS_2 HSs. (a) Optical microscopy images and corresponding atomic stacking configurations of Janus HSs with AA, AB, AAA, AAB, and ABA stackings in the center. Scale bars: 4 μm. Enlarged structures are shown in the second row, where white dashed triangles circumvent the top MoSSe layer, and the black ones in trilayer HSs enclose the middle MoS_2 layer. The top two layers in AAA HSs are indistinguishable under an optical microscope. Scale bars: 1.2 μm. (b) Raman spectra of MoSSe/MoS_2 HSs show the high-frequency modes of Janus MoSSe (J) and MoS_2 (M) components. (c) Raman intensity maps. Left: the A_1' mode of MoSSe (J). Right: the total intensity of the E′ and A_1' modes of MoS_2 (M). Scale bars: 2 μm. (d) LF shear mode (SM) and breathing mode (BM) corresponding to the highlighted region in (b). (e) Illustration of interlayer shear and breathing modes.

from CVD-grown few-layer MoS_2 by in situ selenization where only the top layer of S atoms was replaced by Se atoms. The characteristic E′ and A_1' Raman modes of the MoSSe and MoS_2 constituents in the Raman spectra confirm the successful synthesis of Janus HSs. As compared to pristine bilayer MoS_2, bilayer Janus HSs (MoSSe/MoS_2) exhibit an enhancement of interlayer coupling up to 13.2%, as revealed by experimental LF shear and breathing modes. The overall enhancement can be well explained by a reduced interlayer distance as a result of charge redistribution in the polar Janus MoSSe that contributes to additional Coulombic ion−dipole interactions. The compressive strain in the Janus MoSSe due to lattice mismatch with the bottom MoS_2 layer, as revealed by high-frequency (HF) Raman shifts, also plays an important role in achieving the enhanced interlayer coupling. The effects of both intrinsic dipole and strain on the interlayer coupling have been confirmed by density functional theory (DFT) calculations. Our study reveals the enhanced interlayer interactions in vdW HSs that involve polar Janus TMDs, which will facilitate the design of electronics, optoelectronics, and valleytronics based on the assembly of layered materials where the interlayer coupling is crucial to the device performance.

https://dx.doi.org/10.1021/jacs.0c07051
J. Am. Chem. Soc. 2020, 142, 17499−17507

RESULTS

Polar Janus TMD HS. The synthesis process of monolayer MoSSe and MoSSe/MoS_2 HS is shown in Figure 1b. The CVD-synthesized MoS_2 samples (monolayer, bilayer, and trilayer) are placed in the center of a quartz tube. The top layer of S atoms is stripped off by remote hydrogen plasma and controllably replaced with Se atoms.[13] As shown in Figure 1c, monolayer MoSSe flake maintains the triangular shape with an atomically flat surface as pristine MoS_2. The medium-angle annular dark-field scanning transmission electron microscopy (MAADF-STEM) image shows the hexagonal lattice of monolayer Janus MoSSe corresponding to the crystal structure in Figure 1a. The hexagonal pattern of MoSSe differs from that of MoS_2[33,34] by the higher contrast of Se atoms. The stoichiometric structure of MoSSe can also be distinguished from MoS_2 by Raman and photoluminescence (PL) spectra, which exhibit the A_1' mode at 289.5 cm^{-1} and the E′ mode at 355.0 cm^{-1} and one emission peak at 1.71 eV (Figure 1d,e), respectively, that is consistent with the previous report.[13]

In terms of the MoSSe/MoS_2 HSs (referred to as Janus HSs or simply HSs), there are five configurations including bilayer (AA, AB) and trilayer (AAA, AAB, ABA) HSs as illustrated in Figure 2a, in which AA and AB denote 3R and 2H stackings, respectively. For trilayer HSs, AAB as an example means that the bottom interface (MoS_2/MoS_2) is 3R stacking, while the top interface (MoSSe/MoS_2) is 2H stacking. In Figure 2b, all types of HSs show three prominent HF Raman modes: the A_1' mode around 290 cm^{-1} of the Janus MoSSe constituent (J), the E′ mode around 382−384 cm^{-1}, and the A_1' mode around 405−407 cm^{-1} of the MoS_2 constituent (M). Here, we use the prevalent A_1' and E′ notations to represent the out-of-plane and in-plane lattice vibrations for simplicity. Detailed symmetry labels based on group theory are listed in Tables S1 and S2. To verify the successful conversion of MoSSe/MoS_2 HSs, we performed hyperspectral Raman imaging on the multilayers before (Figures S1−S3) and after Janus conversion (Figure 2c). The number of constituent layers can be easily interpreted from the HF modes of Raman imaging in a fast and nondestructive manner as shown by the AAB HS in Figure 2c. The increase of the number of MoS_2 layer from the periphery to the center (monolayer MoSSe to AA HS to AAB HS) is shown by the stepped Raman intensities of HF modes.[35] On the contrary, the Raman intensity of MoSSe is relatively uniform across the flake, which confirms the complete and uniform selenization of the surface area. In addition to HF features, the Janus HSs exhibit distinct Raman modes in the LF regime (Figure 2d). The LF modes around 22 and 38 cm^{-1} of the bilayer HSs are attributed to interlayer shear and breathing modes, representing in-plane and out-of-plane vibrations between adjacent layers (Figure 2e), respectively.

In Figure 3 we summarize the Raman frequencies and show the difference between HSs and pristine MoS_2 bilayers in detail. The frequency for each measurement shown as the light-colored dots in Figure 3a is the average of Stokes and anti-Stokes mode frequencies (Figure S4). As shown in Figure 3a, left panel, bilayer AA and AB HSs display slight differences in terms of mode frequency. The average shear mode of AA HSs $\omega_S^{AA,HS}$ = 23.0 cm^{-1} is blue-shifted by 0.7 cm^{-1} to that of AB HSs, whereas the average breathing mode $\omega_B^{AA,HS}$ = 38.5 cm^{-1} is red-shifted by 0.8 cm^{-1}. As a reference, pure bilayer MoS_2 also displays the same trend in that the AA MoS_2 shear (breathing) mode frequency is higher (lower) than that of AB

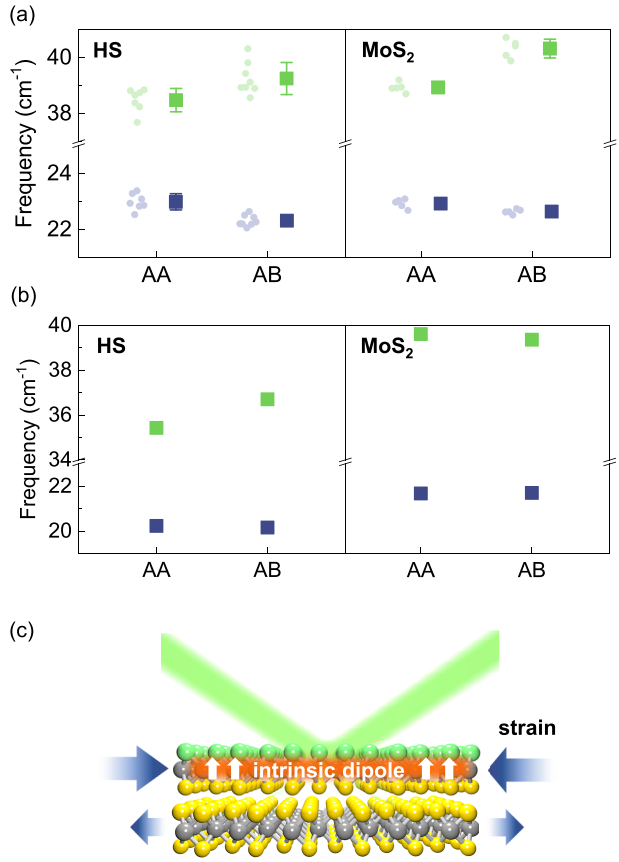

Figure 3. LF modes of bilayer HSs and pristine MoS_2. (a) Experimental shear mode (navy) and breathing mode (green) of HSs and MoS_2. Light-colored dots show the measured values of several samples. Squares are the mean values, and error bars represent the standard deviations of the samples measured. (b) DFT calculations of shear mode (navy) and breathing mode (green) of HSs and MoS_2. (c) Illustration of intrinsic dipole and strain in bilayer Janus HS under laser illumination.

MoS_2 (Figure 3a, right panel). DFT calculations reproduce perfectly the LF modes of bilayer Janus HS and MoS_2 along with their distinctive features as shown in Figure 3b. The similarities between the LF modes of MoS_2 and HS suggest that Janus HSs inherit the crystal configurations and interfacial properties from pristine MoS_2 to some extent. In comparison to pristine MoS_2, the average shear and breathing modes of AA and AB HSs show red-shifts of around 1 cm^{-1} in the experiments, which are also well captured by DFT calculations exhibiting frequency red-shifts of about 2−4 cm^{-1}. The overall decreases in LF mode frequencies of Janus HSs are related to the larger atomic mass of MoSSe and the change in the vdW force between the atomic layers. The LF modes of trilayer HSs summarized in Figure S5 will be discussed later.

Enhanced Interlayer Coupling. From the measured LF Raman modes, we can approximate the interlayer force constant of Janus HSs using the linear chain model:[29]

$$K = (2\pi\omega c)^2\mu \quad (1)$$

Here, K represents the interlayer force constant, ω is the interlayer vibrational frequency, c is the speed of light, and μ is the reduced mass per unit area. The lattice constants of monolayer MoSSe and MoS_2 obtained from MAADF-STEM are both a = 3.16 Å. Hence, the reduced mass per unit area

https://dx.doi.org/10.1021/jacs.0c07051
J. Am. Chem. Soc. 2020, 142, 17499−17507

Table 1. Interlayer Coupling Strength by Linear Chain Model[a]

	force constant	AA HS	AA MoS_2	ΔK^{AA}	AB HS	AB MoS_2	ΔK^{AB}
experiment	K_x (10^{19} N m^{-3})	3.26	2.88	**0.38 (13.2%)**	3.07	2.81	**0.26 (9.3%)**
	K_z (10^{19} N m^{-3})	9.13	8.29	**1.02 (10.1%)**	9.50	8.88	**0.62 (7.0%)**
calculation (a = 3.1 Å)	K_x (10^{19} N m^{-3})	3.00	2.67	**0.33 (12.4%)**	2.98	2.67	**0.31 (11.6%)**
	K_z (10^{19} N m^{-3})	9.21	8.90	**0.31 (3.5%)**	9.88	8.79	**1.09 (12.4%)**

[a]Percentages in the brackets are defined as $\frac{K^{HS} - K^{MoS_2}}{K^{MoS_2}}$.

values for bilayer MoS_2 and Janus HS are approximated to be 1.537×10^{-6} and 1.733×10^{-6} kg m^{-2}, respectively (details in Supporting Information section 3). Table 1 summarizes the in-plane and out-of-plane interlayer force constants K obtained from the LF modes using the linear chain model. Standard deviations of the experimental K are typically a few percentages of the corresponding K values (Table S3). For pristine MoS_2 with AB stacking, the experimental in-plane and out-of-plane interlayer force constants are $K_x^{AB,MoS_2} = 2.81 \times 10^{19}$ N m^{-3} and $K_z^{AB,MoS_2} = 8.88 \times 10^{19}$ N m^{-3}, consistent with mechanically exfoliated 2H MoS_2 multilayers with $K_x = 2.82 \times 10^{19}$ N m^{-3} and $K_z = 8.90 \times 10^{19}$ N m^{-3}.[29] Meanwhile, the interlayer force constants for AB HS are $K_x^{AB,HS} = 3.07 \times 10^{19}$ N m^{-3} and $K_z^{AB,HS} = 9.50 \times 10^{19}$ N m^{-3}, much higher than the corresponding MoS_2 values. Surprisingly, the interfacial force constants of bilayer Janus HSs $K_x^{AA,HS}$, $K_x^{AB,HS}$, $K_z^{AA,HS}$, and $K_z^{AB,HS}$ are all enhanced significantly by 7.0−13.2% as compared to their pristine MoS_2 counterparts, as explicitly shown in Table 1. Furthermore, Table 1 reveals two intriguing features: the enhancement of AA HSs is greater than that of AB HSs, and the absolute increase of K_z (out-of-plane) is higher than the absolute increase of K_x (in-plane).

The observation of both LF modes with strong intensities in our MoSSe/MoS_2 is proof of clean interface and high-symmetry stacking. For most cases of artificially stacked TMD HSs, the interlayer shear mode is not observable as a consequence of an uncontrollable interfacial environment.[36] However, even under optimal interfacial conditions, the interlayer coupling of vdW HSs is generally weaker than that of homobilayers. For example, Zhang et al. reported a MoS_2/WS_2 HS by CVD synthesis,[37] which has a clean interface but without any intrinsic out-of-plane dipole. The shear and breathing modes of their MoS_2/WS_2 HS are reported to be at 18 and 31 cm^{-1}, respectively. Using the linear chain model, interlayer force constants of MoS_2/WS_2 HS are $K_x^{MoS_2/WS_2} = 2.2 \times 10^{19}$ N m^{-3} and $K_z^{MoS_2/WS_2} = 6.4 \times 10^{19}$ N m^{-3}, which are evidently lower than both of bilayer MoS_2 (Table 1) and WS_2 ($K_x^{WS_2} = 3.3 \times 10^{19}$ N m^{-3} and $K_z^{WS_2} = 7.9 \times 10^{19}$ N m^{-3}).[38] This comparison shows that the enhanced interlayer coupling in our polar MoSSe/MoS_2 HSs is fundamentally different from that in nonpolar vdW HSs. Here, we hypothesize that the reason for this enhanced interlayer coupling of Janus HSs involves the modulation of interlayer spacing, which is attributed to the effects of intrinsic dipole and compressive strain of polar Janus MoSSe (Figure 3c).

Origins of the Enhanced Interlayer Coupling. To clarify how interlayer coupling is affected by Janus TMD, we performed DFT calculations with vdW-DF (optB86b-vdW type)[39] correction on bilayer HS and MoS_2 with the lattice constants a = 3.0, 3.1, 3.2, and 3.3 Å. It is worth noting that the theoretical lattice constants a of relaxed MoSSe and MoS_2 monolayers are 3.23 and 3.16 Å. The DFT calculations with a = 3.1 Å yield the increase of interlayer force constant ΔK = 3.5−12.4% as shown in Table 1, which is very close to the experimental values (ΔK = 7.0−13.2%). Additionally, it also gives the most reasonable MoS_2 mode frequencies (Figures S6 and S7). The consistency of experiments and DFT with a = 3.1 Å results suggests that the top Janus MoSSe layer is confined by the original MoS_2 lattice and is subjected to a significant compressive strain due to lattice mismatch. In particular, calculations using other a values do not show the overall enhancement of interlayer coupling (Table S4), which implies that the compressive strain in Janus MoSSe is critical in forming an enhanced interlayer interaction. To provide a better understanding, the calculated lattice constant a and the interlayer distance of the relaxed monolayers and HSs are listed in Table S5.

The interlayer spacing d_{Mo}, defined as the Mo−Mo distance along the z direction, is reduced after heterostacking and is directly related to the enhancement of interlayer interactions. According to DFT calculations, d_{Mo} of the HS is always smaller than that of MoS_2 (Figure 4a,b). Thus, the enhancement of interlayer coupling after Janus conversion is explicitly explained by the reduced interlayer spacing of polar Janus HSs in comparison to that of pristine MoS_2. We use Δ to represent the absolute decrease of each parameter after heterostacking, for example, $\Delta d_{Mo} = d_{Mo}(MoS_2) - d_{Mo}(HS)$. The decrease of interlayer spacing Δd_{Mo} for AA and AB HS with a = 3.0−3.3 Å is around 0.01−0.02 Å as shown in Figure 4a. For a = 3.1 Å corresponding to the experimental lattice constant, Δd_{Mo} of AB HS is much smaller than that of AA HS by around 50%. This is consistent with the experimental observation that AB HSs have less enhancement of interlayer coupling than do AA HSs (Table 1). It also suggests that interlayer coupling in polar Janus HS is extremely sensitive to the microscopic interfacial configuration. Using five different types of vdW corrections in DFT, the reduced interlayer spacing is perfectly replicated for bilayer Janus HSs with a = 3.1 Å (Figure S8).

The interlayer spacing comprises three parts: Mo−S distance in the bottom MoS_2 (d_2), interfacial S−S distance (d_S), and S−Mo distance in the top MoSSe (d_3), among which d_2 is mostly unaffected by selenization (Figure S9). Comparing AA and AB stackings for a = 3.0−3.1 Å, Δd_S is the parameter that shows the obvious difference (Figure S9c,d), while Δd_2 and Δd_3 do not change much between AA and AB (Figure S9a,b,e,f). Hence, the different enhancement behaviors between AA and AB HSs can be explained by the modulation of d_S. On another note, Δd_3 is solely dictated by the top Janus layer rather than the nanoscale stacking geometry, because its value is almost the same for AA and AB HSs (Figure S9e,f). In MoSSe, structural asymmetry changes the distribution of the p orbitals of S and Se atoms protruding outside the layer. As a consequence, electrons are more likely to reside at the S side. As shown in Figure 4c,d, the intrinsic dipole moment between S and Se atoms in MoSSe greatly rearranges the atomic configuration and shortens the S−Mo distance d_3 by around 0.01 Å in comparison with d_7 of bilayer MoS_2. The shortened S−Mo distance brings about a decreased Mo−Mo distance d_{Mo}

https://dx.doi.org/10.1021/jacs.0c07051
J. Am. Chem. Soc. 2020, 142, 17499−17507

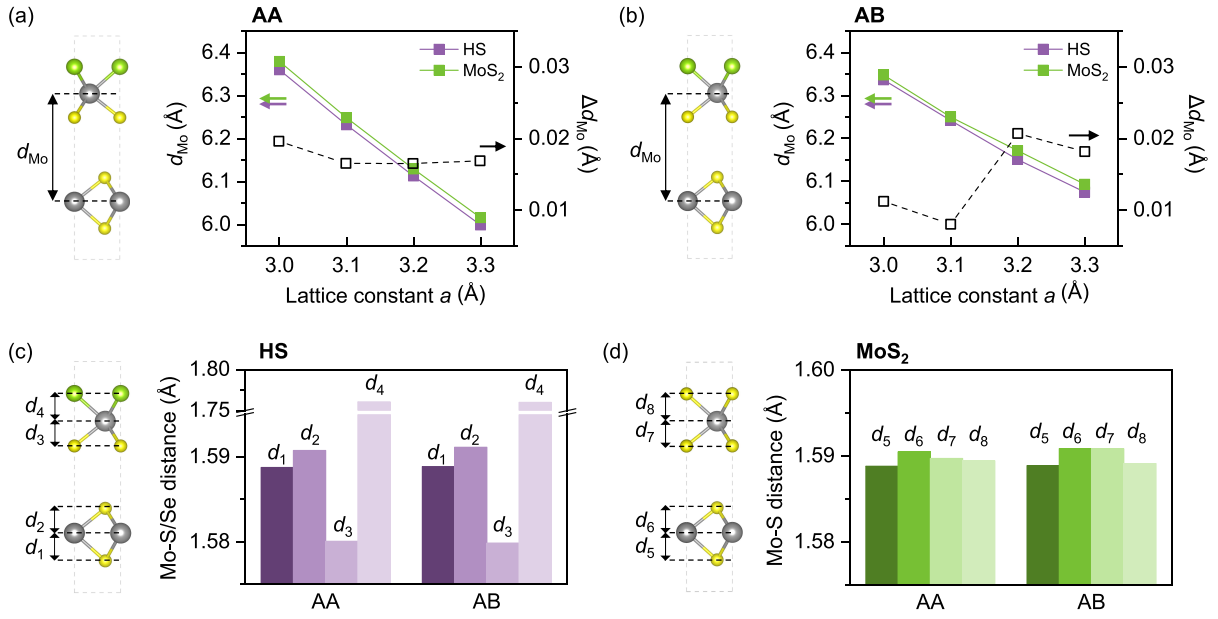

Figure 4. Interlayer spacing by DFT calculations. (a,b) Interlayer spacing d_{Mo} of Janus HS (purple) and pristine MoS_2 (green) with (a) AA and (b) AB stackings for lattice constant a = 3.0−3.3 Å. d_{Mo} is defined as the distance along the z direction between Mo atoms in the two layers. The open squares present the absolute decrease in interlayer spacing after selenization. $\Delta d_{Mo} = d_{Mo}(MoS_2) - d_{Mo}(HS)$. (c,d) Mo−S and Mo−Se distances of bilayer (c) HSs and (d) MoS_2 for a = 3.1 Å. Columns from left to right are the Mo−S and Mo−Se distances in the z direction from bottom to top.

that causes enhanced interlayer interactions (Figure 4a,b). The asymmetric charge density distribution has been theoretically predicted in several Janus TMD related HSs such as MoSSe/WSe_2,[21,40] MoSSe/graphene,[41] and multilayer Janus TMDs.[42] Above all, the origin of enhanced interlayer coupling can be explicitly explained by the modulated atomic interlayer spacing d_{Mo} as a result of the intrinsic dipole moment.

An alternative way to understand the reduced interlayer spacing d_{Mo} is through Coulombic ion−dipole and dipole−dipole interactions (details in Supporting Information section 5). The intrinsic dipole moment of monolayer MoSSe is predicted to be 0.033 |e|·Å by DFT calculations pointing from S to Se where e is the unit charge. The electric field of the dipole moment is expressed as $\vec{E}(R) = K_e\frac{3(\vec{p}\cdot\hat{R})\hat{R} - \vec{p}}{R^3}$, where $\vec{p}$ denotes the dipole moment, R is the distance between the ion and dipole with $\hat{R}$ as the unit vector, and $K_e = \frac{1}{4\pi\varepsilon_0}$. Bader charge analysis[43] predicts that the Mo ion in the bottom layer possesses 1.21|e| positive charges (Table S6). Consequently, the attractive force between the intrinsic dipole and the bottom Mo ion is around $F_{Mo\text{-}int} = 7.29 \times 10^{-12}$ N, which translates to a displacement of −0.009 Å. Besides, DFT calculations indicate that a dipole moment of 0.007 |e|·Å is induced in the bottom nonpolar MoS_2 layer in Janus HS (Figure S10), which increases the Mo−Mo distance by 0.002 Å. Taking both ion−dipole and dipole−dipole interactions into consideration, they lead to a total decrease of Mo−Mo distance by 0.007 Å, consistent with the DFT result of Δd_{Mo} = 0.009 Å for AB HS (Figure 4b). Conclusively, we show that the intrinsic dipole moment in Janus MoSSe takes up a significant role in reducing the interlayer distance, which thus strengthens the interlayer coupling of the polar Janus HS.

In terms of trilayer HSs, one LF Raman peak can be observed at around 28 cm^{-1} for all three stackings (Figure 2d), which resembles the degenerate shear and breathing modes in trilayer MoS_2 (Figure S2).[26−29] Among the trilayer HSs, only the LF modes of AAA HSs are blue-shifted by 1.8 cm^{-1} as compared to that of pure trilayer MoS_2 (Figure S5). Similar to the case of bilayers, this observation validates that Janus heterostacking favors AA stacking over AB stacking because the interface between top MoSSe and middle MoS_2 in AAA HSs is still AA stacking as opposed to the AB interfaces of AAB and ABA HSs. DFT calculations reproduce the LF mode frequencies of trilayer HSs (Figure S5c), in which shear and breathing modes of AAA HS have a splitting of 2.1 cm^{-1}, consistent with the larger line width of LF modes of AAA HSs (Figure 2d). Calculations also reveal that the interlayer spacing between top MoSSe and middle MoS_2 is smaller than the spacing between two bottom MoS_2 for the trilayer HSs (Figure S11). Expectedly, AAA HS has a smaller interfacial distance between the top MoSSe and the middle MoS_2 than do AAB and ABA HSs, which further supports our comparison between AA and AB stackings.

Strain in Janus HS. The predicted strain condition in Janus HSs, that is, compressive strain in MoSSe, is reflected by the frequency-shifts of HF Raman modes (Figure 5). The average MoSSe (J) A_1' mode for bilayer AA and AB HSs is at 290.8 and 291.0 cm^{-1}, while it shifts to a lower frequency around 290.0 cm^{-1} for trilayer HSs (Figure 5a). All of them are at higher frequencies than the A_1' mode of monolayer MoSSe (289.5 cm^{-1}). The blue-shifts of the A_1' mode are consistent with our DFT calculations shown in Figure 5d. DFT calculations also suggest that the A_1' mode of monolayer MoSSe blue-shifts (red-shifts) under compressive (tensile) strain, similar to conventional TMDs (Figure S12a). Thus, it can be inferred that the MoSSe constituent in Janus HSs suffers from compressive strain, and the compressive strain of bilayer HSs is stronger than that of trilayer HSs because the middle MoS_2 layer in the trilayer HS serves as an additional strain buffer.

https://dx.doi.org/10.1021/jacs.0c07051
J. Am. Chem. Soc. 2020, 142, 17499−17507

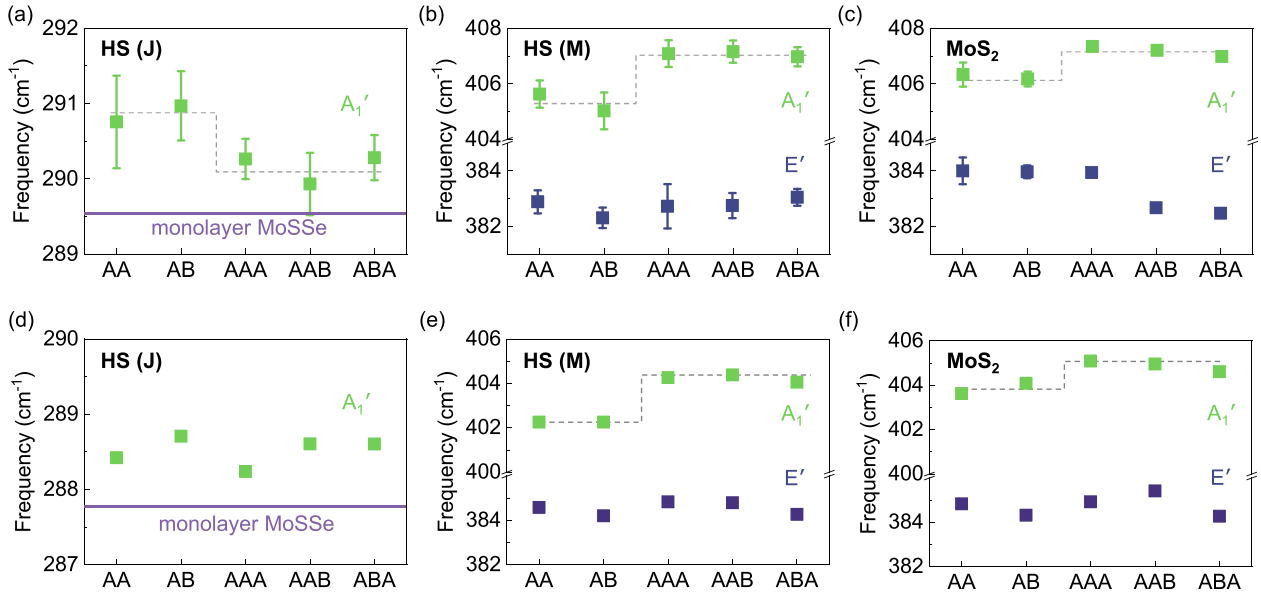

Figure 5. HF Raman modes of HSs and pristine MoS_2. (a,b) Experimental results of (a) the Janus MoSSe (J) A_1' mode frequency and (b) the MoS_2 (M) E′ and A_1' mode frequencies of Janus HSs. The purple line indicates the experimental A_1' mode frequency of an individual MoSSe monolayer. (c) The MoS_2 (M) E′ and A_1' mode frequencies of pristine MoS_2. Some error bars are too small to be visible. (d–f) DFT calculations of the HF modes corresponding to the experimental values in (a)–(c).

Next, we examine the strain in the MoS_2 component by comparing the MoS_2 (M) A_1' and E′ modes of HSs to those of pure MoS_2 (Figure 5b,c). For bilayer HSs, both (M) E′ and A_1' modes for AA and AB HSs are relatively red-shifted by around 1 cm^{-1} as compared to those of pure MoS_2, which is consistent with our DFT calculations (Figure 5e,f) and can be explained by a tensile strain in the MoS_2 component.[44−46] Previous work reported that red-shifts of the E′ mode by 2 cm^{-1} and the A_1' mode by 1 cm^{-1} correspond to 0.4% tensile strain in bilayer MoS_2,[47] which means a change of 0.01 Å in lattice constant. This amount of tensile strain is difficult to be captured by the STEM measurement directly. The tensile strain in the MoS_2 component can be attributed partly to the lattice mismatch from top MoSSe and to the global tensile strain due to the thermal expansion coefficient difference between MoS_2 and SiO_2 substrate.[48] As for the trilayer HSs, the MoS_2 (M) frequency differences between HSs and pure MoS_2 are much smaller, which indicate the strain is less prominent in trilayer HSs than in bilayer HSs. In particular, both the experimental and the theoretical (M) A_1' modes of HSs and pure MoS_2 display blue-shifts from bilayer to trilayer by 2 and 1 cm^{-1}, respectively, as shown by the dashed lines in Figure 5b,c and e,f. Similar features have been reported in graphene/MoS_2 HSs in that the A_1' mode frequency increases from 403 to 405 cm^{-1} when the bottom MoS_2 changes from monolayer to bilayer,[34] which is explained by a higher restoring force in trilayer HSs.

CONCLUSION

We present an unprecedented enhancement in the interlayer coupling of vdW HSs (MoSSe/MoS_2) that involves the polar Janus TMD MoSSe, whose complete and uniform conversion has been proved by HF Raman measurements. In the Raman LF regime, both shear and breathing modes of MoSSe/MoS_2 HSs are observed with frequencies in agreement with our DFT calculations. Unlike previously reported vdW HSs where the interlayer coupling is weaker than homobilayers, we show that the interlayer coupling strength of MoSSe/MoS_2 HSs is enhanced significantly as compared to that of the pure MoS_2 counterparts. This enhancement is directly explained by a reduced interlayer distance d_{Mo} as a result of intrinsic dipole moment using DFT calculations, which can be understood through Coulombic ion−dipole interactions. DFT calculation also shows that the compressive strain in MoSSe is essential for determining the enhanced interlayer force constant. The anticipated compressive strain in MoSSe and tensile strain in MoS_2 are revealed by the experimental and calculated HF Raman modes. Our work unfolds the enhancement of the interfacial coupling in MoSSe/MoS_2 HSs due to Janus heterostacking, which is fundamentally different from nonpolar vdW HSs. Such abnormal interlayer coupling is essential for engineering electronic and optoelectronic devices utilizing vdW heterostacking. By modulating the intrinsic dipole moment in Janus TMD related HSs, carrier transport and electron−hole recombination dynamics can be tuned through the strengthened interlayer coupling, which facilitates future applications such as light detection, catalysis, and energy harvesting.

METHODS

Material Synthesis. Monolayer MoSSe/monolayer MoS_2 (bilayer HS) and monolayer MoSSe/bilayer MoS_2 (trilayer HS) were synthesized by direct selenization of CVD grown bilayer and trilayer MoS_2. The pristine bilayer and trilayer MoS_2 on SiO_2/Si substrates were placed in the middle of a quartz tube in a furnace, and the selenium powder was placed at the upstream of the quartz tube. Before the sulfur stripping process, the base pressure was pumped down to 10 mTorr to remove the residual air in the system. Hydrogen plasma with a power density of 50 W and H_2 flow of 20 sccm were used to strip off the top-layer sulfur atoms. Similar to the previous method,[13] the selenium atoms replaced the sulfur atoms. The plasma-assisted CVD selenization only converted the top surface sulfur, while the second and third layers of MoS_2 covered by the first layer were well protected, to result in MoSSe/MoS_2 HSs.

STEM Measurement. The atomic structure of the sample was observed using the aberration-corrected Nion UltraSTEM 100 at the

https://dx.doi.org/10.1021/jacs.0c07051
J. Am. Chem. Soc. 2020, 142, 17499−17507

Oak Ridge National Laboratory's Center for Nanophase Materials Sciences User Facility operated at 60 kV. In a standard treatment, the sample was baked in a vacuum at 160 °C for 8 h before insertion into the microscope column. The vacuum level at the sample volume during the experiments was $<3 \times 10^{-9}$ mbar. The convergence semiangle of the electron probe is 30 mrad, and the collection semiangle of the electron energy loss spectrum is 48 mrad. The medium angle annular dark field (MAADF) collection semiangle range is 54−200 mrad. Electron current was kept between 50 and 60 pA during all of the imaging.

Optical Measurement. Raman measurements were performed on a Horiba Labram spectrometer with an excitation wavelength of 532 nm. A 100× objective was used to focus the laser and collect the scattered light. Laser power was controlled below 0.1 mW to avoid local heating and oxidation of the samples. Both Stokes and anti-Stokes Raman scattering were measured and averaged to obtain accurate values of the Raman mode frequencies. A 1800/mm grating in the Raman spectrometer and numerical fitting of the measured Raman spectra offer a spectral accuracy of 0.1 cm^{-1}. PL measurements were performed on the same setup with the same acquisition parameters.

DFT Calculations. We have employed the first-principles DFT calculations for the simulations of the mechanical and electronic properties of the Janus HS, implemented in the Vienna ab initio simulation package (VASP).[49,50] The Projector Augmented-Wave method[51] was used for the pseudopotential formalism, and the Perdew−Burke−Ernzerhof (PBE)[52] parametrized functional with vdW-DF (optB86b-vdW type) corrections[39] was used for the exchange-correlation (x-c) energy. A vacuum region with a thickness of around 15 Å was included to reduce the interaction between repeated units in the slab geometry under periodic boundary condition. The structures were fully relaxed until the forces were smaller than 5×10^{-4} eV/Å. The calculations were converged with an energy cutoff 500 eV and a Γ-centered $23 \times 23 \times 1$ Monkhorst−Pack *k*-mesh grid. The phonon modes at Γ point were evaluated by deriving the Hessian matrix within the density functional perturbation theory (DFPT). The DFT results using the vdW-DF (optB86b-vdW type) corrections[39] with DFPT can be replicated using other x-c functionals, including the DFT-D3 with zero damping,[53] DFT-D3 with Becke−Johnson damping,[54] and the original vdW-DF (optB86b-vdW type)[39] with finite difference method to calculate the Γ point phonons as shown in Figures S13 and S14 and Table S7.

■ ASSOCIATED CONTENT

Supporting Information

The Supporting Information is available free of charge at https://pubs.acs.org/doi/10.1021/jacs.0c07051.

Symmetry assignment of the Raman modes, experimental Raman spectra, and DFT calculations using different x-c functionals (PDF)

■ AUTHOR INFORMATION

Corresponding Authors

Yunfan Guo − *Department of Electrical Engineering and Computer Science, Massachusetts Institute of Technology, Cambridge, Massachusetts 02139, United States*; Email: yfguo112@mit.edu

Jing Kong − *Department of Electrical Engineering and Computer Science, Massachusetts Institute of Technology, Cambridge, Massachusetts 02139, United States*; orcid.org/0000-0003-0551-1208; Email: jingkong@mit.edu

Shengxi Huang − *Department of Electrical Engineering, The Pennsylvania State University, University Park, Pennsylvania 16802, United States*; orcid.org/0000-0002-3618-9074; Email: sjh5899@psu.edu

Authors

Kunyan Zhang − *Department of Electrical Engineering, The Pennsylvania State University, University Park, Pennsylvania 16802, United States*; orcid.org/0000-0002-6830-409X

Qingqing Ji − *Department of Electrical Engineering and Computer Science, Massachusetts Institute of Technology, Cambridge, Massachusetts 02139, United States*; orcid.org/0000-0001-5526-3746

Ang-Yu Lu − *Department of Electrical Engineering and Computer Science, Massachusetts Institute of Technology, Cambridge, Massachusetts 02139, United States*

Cong Su − *Department of Nuclear and Materials Science and Engineering, Massachusetts Institute of Technology, Cambridge, Massachusetts 02139, United States*

Hua Wang − *Department of Materials Science and Engineering, Texas A&M University, College Station, Texas 77843, United States*

Alexander A. Puretzky − *Center for Nanophase Materials Sciences, Oak Ridge National Laboratory, Oak Ridge, Tennessee 37831, United States*; orcid.org/0000-0002-9996-4429

David B. Geohegan − *Center for Nanophase Materials Sciences, Oak Ridge National Laboratory, Oak Ridge, Tennessee 37831, United States*

Xiaofeng Qian − *Department of Materials Science and Engineering, Texas A&M University, College Station, Texas 77843, United States*; orcid.org/0000-0003-1627-288X

Shiang Fang − *Department of Physics and Astronomy, Center for Materials Theory, Rutgers University, New Jersey 08854, United States*

Efthimios Kaxiras − *Department of Physics and John A. Paulson School of Engineering and Applied Sciences, Harvard University, Cambridge, Massachusetts 02138, United States*

Complete contact information is available at: https://pubs.acs.org/10.1021/jacs.0c07051

Author Contributions

#K.Z., Y.G., and Q.J. contributed equally.

Notes

The authors declare no competing financial interest.

■ ACKNOWLEDGMENTS

K.Z. acknowledges the support from Milton and Albertha Langdon Memorial Graduate Fellowship. The early stage development of Janus structures (Y.G.) was supported by the Air Force Office of Scientific Research under the MURI-FATE program, grant number FA9550-15-1-0514, the later stage of the Janus structure conversion and characterization (Y.G.) was support by U.S. Department of Energy, Office of Science, Basic Energy Sciences, award number DESC0020042. The CVD MoS2 materials were synthesis by Q.J. with the support from the STC Center for Integrated Quantum Materials, National Science Foundation, grant number DMR-1231319. A.-Y. L. assisted the setup to convert Janus materials and characterizations and was supported by the U.S. Army Research Office through the Institute for Soldier Nanotechnologies at MIT, under contract number W911NF-18-2-0048. C.S. collected the STEM characterization of Janus materials and was support by U.S. Army Research Office under grant number W911NF-18-1-0431. H.W. and X.Q. acknowledge the support from the National Science Foundation under grant number DMR-1753054. S.F. is supported by a Rutgers Center for Material Theory Distinguished Postdoctoral Fellowship. E.K. acknowl-

edges the support from STC Center for Integrated Quantum Materials, National Science Foundation, grant number DMR-1231319. S.H. acknowledges the support from the National Science Foundation under grant number ECCS-1943895.

REFERENCES

(1) Po, H. C.; Zou, L.; Vishwanath, A.; Senthil, T. Origin of Mott insulating behavior and superconductivity in twisted bilayer graphene. *Phys. Rev. X* **2018**, *8* (3), 031089.
(2) Cao, Y.; Fatemi, V.; Demir, A.; Fang, S.; Tomarken, S. L.; Luo, J. Y.; Sanchez-Yamagishi, J. D.; Watanabe, K.; Taniguchi, T.; Kaxiras, E.; Ashoori, R. C.; Jarillo-Herrero, P. Correlated insulator behaviour at half-filling in magic-angle graphene superlattices. *Nature* **2018**, *556* (7699), 80−84.
(3) Xu, C.; Balents, L. Topological superconductivity in twisted multilayer graphene. *Phys. Rev. Lett.* **2018**, *121* (8), 087001.
(4) Cao, Y.; Fatemi, V.; Fang, S.; Watanabe, K.; Taniguchi, T.; Kaxiras, E.; Jarillo-Herrero, P. Unconventional superconductivity in magic-angle graphene superlattices. *Nature* **2018**, *556* (7699), 43−50.
(5) Hu, G.; Ou, Q.; Si, G.; Wu, Y.; Wu, J.; Dai, Z.; Krasnok, A.; Mazor, Y.; Zhang, Q.; Bao, Q.; Qiu, C.-W.; Alù, A. Topological polaritons and photonic magic angles in twisted α-MoO_3 bilayers. *Nature* **2020**, *582* (7811), 209−213.
(6) Serlin, M.; Tschirhart, C. L.; Polshyn, H.; Zhang, Y.; Zhu, J.; Watanabe, K.; Taniguchi, T.; Balents, L.; Young, A. F. Intrinsic quantized anomalous Hall effect in a moiré heterostructure. *Science* **2020**, *367* (6480), 900.
(7) Tran, K.; Moody, G.; Wu, F.; Lu, X.; Choi, J.; Kim, K.; Rai, A.; Sanchez, D. A.; Quan, J.; Singh, A.; Embley, J.; Zepeda, A.; Campbell, M.; Autry, T.; Taniguchi, T.; Watanabe, K.; Lu, N.; Banerjee, S. K.; Silverman, K. L.; Kim, S.; Tutuc, E.; Yang, L.; MacDonald, A. H.; Li, X. Evidence for moiré excitons in van der Waals heterostructures. *Nature* **2019**, *567* (7746), 71−75.
(8) Seyler, K. L.; Rivera, P.; Yu, H.; Wilson, N. P.; Ray, E. L.; Mandrus, D. G.; Yan, J.; Yao, W.; Xu, X. Signatures of moiré-trapped valley excitons in $MoSe_2$/WSe_2 heterobilayers. *Nature* **2019**, *567* (7746), 66−70.
(9) Jin, C.; Regan, E. C.; Yan, A.; Iqbal Bakti Utama, M.; Wang, D.; Zhao, S.; Qin, Y.; Yang, S.; Zheng, Z.; Shi, S.; Watanabe, K.; Taniguchi, T.; Tongay, S.; Zettl, A.; Wang, F. Observation of moiré excitons in WSe_2/WS_2 heterostructure superlattices. *Nature* **2019**, *567* (7746), 76−80.
(10) Cheng, Y. C.; Zhu, Z. Y.; Tahir, M.; Schwingenschlögl, U. Spin-orbit−induced spin splittings in polar transition metal dichalcogenide monolayers. *EPL (Europhysics Letters)* **2013**, *102* (5), 57001.
(11) Cheng, C.; Sun, J.-T.; Chen, X.-R.; Fu, H.-X.; Meng, S. Nonlinear Rashba spin splitting in transition metal dichalcogenide monolayers. *Nanoscale* **2016**, *8* (41), 17854−17860.
(12) Defo, R. K.; Fang, S.; Shirodkar, S. N.; Tritsaris, G. A.; Dimoulas, A.; Kaxiras, E. Strain dependence of band gaps and exciton energies in pure and mixed transition-metal dichalcogenides. *Phys. Rev. B: Condens. Matter Mater. Phys.* **2016**, *94* (15), 155310.
(13) Lu, A.-Y.; Zhu, H.; Xiao, J.; Chuu, C.-P.; Han, Y.; Chiu, M.-H.; Cheng, C.-C.; Yang, C.-W.; Wei, K.-H.; Yang, Y.; Wang, Y.; Sokaras, D.; Nordlund, D.; Yang, P.; Muller, D. A.; Chou, M.-Y.; Zhang, X.; Li, L.-J. Janus monolayers of transition metal dichalcogenides. *Nat. Nanotechnol.* **2017**, *12*, 744.
(14) Zhang, J.; Jia, S.; Kholmanov, I.; Dong, L.; Er, D.; Chen, W.; Guo, H.; Jin, Z.; Shenoy, V. B.; Shi, L.; Lou, J. Janus monolayer transition-metal dichalcogenides. *ACS Nano* **2017**, *11* (8), 8192−8198.
(15) Lin, Y.-C.; Liu, C.; Yu, Y.; Zarkadoula, E.; Yoon, M.; Puretzky, A. A.; Liang, L.; Kong, X.; Gu, Y.; Strasser, A.; Meyer, H. M.; Lorenz, M.; Chisholm, M. F.; Ivanov, I. N.; Rouleau, C. M.; Duscher, G.; Xiao, K.; Geohegan, D. B. Low energy implantation into transition-metal dichalcogenide monolayers to form Janus structures. *ACS Nano* **2020**, *14* (4), 3896−3906.
(16) Dong, L.; Lou, J.; Shenoy, V. B. Large in-plane and vertical piezoelectricity in Janus transition metal dichalchogenides. *ACS Nano* **2017**, *11* (8), 8242−8248.
(17) Jia, S.; Bandyopadhyay, A.; Kumar, H.; Zhang, J.; Wang, W.; Zhai, T.; Shenoy, V. B.; Lou, J. Biomolecular sensing by surface-enhanced Raman scattering of monolayer Janus transition metal dichalcogenide. *Nanoscale* **2020**, *12* (19), 10723−10729.
(18) Riis-Jensen, A. C.; Pandey, M.; Thygesen, K. S. Efficient charge separation in 2D Janus van der Waals structures with built-in electric fields and intrinsic p−n doping. *J. Phys. Chem. C* **2018**, *122* (43), 24520−24526.
(19) Jin, H.; Wang, T.; Gong, Z.-R.; Long, C.; Dai, Y. Prediction of an extremely long exciton lifetime in a Janus-MoSTe monolayer. *Nanoscale* **2018**, *10* (41), 19310−19315.
(20) Guan, Z.; Ni, S.; Hu, S. Tunable electronic and optical properties of monolayer and multilayer Janus MoSSe as a photocatalyst for solar water splitting: a first-principles study. *J. Phys. Chem. C* **2018**, *122* (11), 6209−6216.
(21) Liang, Y.; Li, J.; Jin, H.; Huang, B.; Dai, Y. Photoexcitation dynamics in Janus-MoSSe/WSe_2 heterobilayers: *ab initio* time-domain study. *J. Phys. Chem. Lett.* **2018**, *9* (11), 2797−2802.
(22) Yagmurcukardes, M.; Qin, Y.; Ozen, S.; Sayyad, M.; Peeters, F. M.; Tongay, S.; Sahin, H. Quantum properties and applications of 2D Janus crystals and their superlattices. *Appl. Phys. Rev.* **2020**, *7* (1), 011311.
(23) Li, Y.; Qin, J.-K.; Xu, C.-Y.; Cao, J.; Sun, Z.-Y.; Ma, L.-P.; Hu, P. A.; Ren, W.; Zhen, L. Electric field tunable interlayer relaxation process and interlayer coupling in WSe_2/graphene heterostructures. *Adv. Funct. Mater.* **2016**, *26* (24), 4319−4328.
(24) Wu, S.; Ross, J. S.; Liu, G.-B.; Aivazian, G.; Jones, A.; Fei, Z.; Zhu, W.; Xiao, D.; Yao, W.; Cobden, D.; Xu, X. Electrical tuning of valley magnetic moment through symmetry control in bilayer MoS_2. *Nat. Phys.* **2013**, *9*, 149.
(25) Song, Z.; Quhe, R.; Liu, S.; Li, Y.; Feng, J.; Yang, Y.; Lu, J.; Yang, J. Tunable valley polarization and valley orbital magnetic moment Hall effect in honeycomb systems with broken inversion symmetry. *Sci. Rep.* **2015**, *5*, 13906.
(26) Zhao, Y.; Luo, X.; Li, H.; Zhang, J.; Araujo, P. T.; Gan, C. K.; Wu, J.; Zhang, H.; Quek, S. Y.; Dresselhaus, M. S.; Xiong, Q. Interlayer breathing and shear modes in few-trilayer MoS_2 and WSe_2. *Nano Lett.* **2013**, *13* (3), 1007−1015.
(27) Lu, X.; Utama, M. I. B.; Lin, J.; Luo, X.; Zhao, Y.; Zhang, J.; Pantelides, S. T.; Zhou, W.; Quek, S. Y.; Xiong, Q. Rapid and nondestructive identification of polytypism and stacking sequences in few-layer molybdenum diselenide by Raman spectroscopy. *Adv. Mater.* **2015**, *27* (30), 4502−4508.
(28) Luo, X.; Lu, X.; Cong, C.; Yu, T.; Xiong, Q.; Ying Quek, S. Stacking sequence determines Raman intensities of observed interlayer shear modes in 2D layered materials − a general bond polarizability model. *Sci. Rep.* **2015**, *5*, 14565.
(29) Zhang, X.; Han, W. P.; Wu, J. B.; Milana, S.; Lu, Y.; Li, Q. Q.; Ferrari, A. C.; Tan, P. H. Raman spectroscopy of shear and layer breathing modes in multilayer MoS_2. *Phys. Rev. B: Condens. Matter Mater. Phys.* **2013**, *87* (11), 115413.
(30) Puretzky, A. A.; Liang, L.; Li, X.; Xiao, K.; Wang, K.; Mahjouri-Samani, M.; Basile, L.; Idrobo, J. C.; Sumpter, B. G.; Meunier, V.; Geohegan, D. B. Low-frequency Raman fingerprints of two-dimensional metal dichalcogenide layer stacking configurations. *ACS Nano* **2015**, *9* (6), 6333−6342.
(31) Ling, X.; Liang, L.; Huang, S.; Puretzky, A. A.; Geohegan, D. B.; Sumpter, B. G.; Kong, J.; Meunier, V.; Dresselhaus, M. S. Low-frequency interlayer breathing modes in few-layer black phosphorus. *Nano Lett.* **2015**, *15* (6), 4080−4088.
(32) Luo, X.; Lu, X.; Koon, G. K. W.; Castro Neto, A. H.; Özyilmaz, B.; Xiong, Q.; Quek, S. Y. Large frequency change with thickness in interlayer breathing mode—significant interlayer interactions in few layer black phosphorus. *Nano Lett.* **2015**, *15* (6), 3931−3938.
(33) van der Zande, A. M.; Huang, P. Y.; Chenet, D. A.; Berkelbach, T. C.; You, Y.; Lee, G.-H.; Heinz, T. F.; Reichman, D. R.; Muller, D.

A.; Hone, J. C. Grains and grain boundaries in highly crystalline monolayer molybdenum disulphide. *Nat. Mater.* **2013**, *12*, 554.
(34) Gong, Y.; Lin, J.; Wang, X.; Shi, G.; Lei, S.; Lin, Z.; Zou, X.; Ye, G.; Vajtai, R.; Yakobson, B. I.; Terrones, H.; Terrones, M.; Tay Beng, K.; Lou, J.; Pantelides, S. T.; Liu, Z.; Zhou, W.; Ajayan, P. M. Vertical and in-plane heterostructures from WS_2/MoS_2 monolayers. *Nat. Mater.* **2014**, *13*, 1135.
(35) Castellanos-Gomez, A.; Quereda, J.; van der Meulen, H. P.; Agraït, N.; Rubio-Bollinger, G. Spatially resolved optical absorption spectroscopy of single- and few-layer MoS_2 by hyperspectral imaging. *Nanotechnology* **2016**, *27* (11), 115705.
(36) Lui, C. H.; Ye, Z.; Ji, C.; Chiu, K.-C.; Chou, C.-T.; Andersen, T. I.; Means-Shively, C.; Anderson, H.; Wu, J.-M.; Kidd, T.; Lee, Y.-H.; He, R. Observation of interlayer phonon modes in van der Waals heterostructures. *Phys. Rev. B: Condens. Matter Mater. Phys.* **2015**, *91* (16), 165403.
(37) Zhang, J.; Wang, J.; Chen, P.; Sun, Y.; Wu, S.; Jia, Z.; Lu, X.; Yu, H.; Chen, W.; Zhu, J.; Xie, G.; Yang, R.; Shi, D.; Xu, X.; Xiang, J.; Liu, K.; Zhang, G. Observation of strong interlayer coupling in MoS_2/WS_2 heterostructures. *Adv. Mater.* **2016**, *28* (10), 1950−1956.
(38) Chen, S.-Y.; Zheng, C.; Fuhrer, M. S.; Yan, J. Helicity-resolved Raman scattering of MoS_2, $MoSe_2$, WS_2, and WSe_2 atomic layers. *Nano Lett.* **2015**, *15* (4), 2526−2532.
(39) Klimeš, J.; Bowler, D. R.; Michaelides, A. van der Waals density functionals applied to solids. *Phys. Rev. B: Condens. Matter Mater. Phys.* **2011**, *83* (19), 195131.
(40) Long, C.; Gong, Z.-R.; Jin, H.; Dai, Y. Observation of intrinsic dark exciton in Janus-MoSSe heterosturcture induced by intrinsic electric field. *J. Phys.: Condens. Matter* **2018**, *30* (39), 395001.
(41) Li, Y.; Wang, J.; Zhou, B.; Wang, F.; Miao, Y.; Wei, J.; Zhang, B.; Zhang, K. Tunable interlayer coupling and Schottky barrier in graphene and Janus MoSSe heterostructures by applying an external field. *Phys. Chem. Chem. Phys.* **2018**, *20* (37), 24109−24116.
(42) Song, B.; Liu, L.; Yam, C. Suppressed carrier recombination in Janus MoSSe bilayer stacks: a time-domain *ab initio* study. *J. Phys. Chem. Lett.* **2019**, *10* (18), 5564−5570.
(43) Henkelman, G.; Arnaldsson, A.; Jónsson, H. A fast and robust algorithm for Bader decomposition of charge density. *Comput. Mater. Sci.* **2006**, *36* (3), 354−360.
(44) Hui, Y. Y.; Liu, X.; Jie, W.; Chan, N. Y.; Hao, J.; Hsu, Y.-T.; Li, L.-J.; Guo, W.; Lau, S. P. Exceptional tunability of band energy in a compressively strained trilayer MoS_2 sheet. *ACS Nano* **2013**, *7* (8), 7126−7131.
(45) Rice, C.; Young, R. J.; Zan, R.; Bangert, U.; Wolverson, D.; Georgiou, T.; Jalil, R.; Novoselov, K. S. Raman-scattering measurements and first-principles calculations of strain-induced phonon shifts in monolayer MoS_2. *Phys. Rev. B: Condens. Matter Mater. Phys.* **2013**, *87* (8), 081307.
(46) Castellanos-Gomez, A.; Roldán, R.; Cappelluti, E.; Buscema, M.; Guinea, F.; van der Zant, H. S. J.; Steele, G. A. Local strain engineering in atomically thin MoS_2. *Nano Lett.* **2013**, *13* (11), 5361−5366.
(47) Lee, J.-U.; Woo, S.; Park, J.; Park, H. C.; Son, Y.-W.; Cheong, H. Strain-shear coupling in bilayer MoS_2. *Nat. Commun.* **2017**, *8* (1), 1370.
(48) Plechinger, G.; Mann, J.; Preciado, E.; Barroso, D.; Nguyen, A.; Eroms, J.; Schüller, C.; Bartels, L.; Korn, T. A direct comparison of CVD-grown and exfoliated MoS_2 using optical spectroscopy. *Semicond. Sci. Technol.* **2014**, *29* (6), 064008.
(49) Kresse, G.; Furthmüller, J. Efficient iterative schemes for *ab initio* total-energy calculations using a plane-wave basis set. *Phys. Rev. B: Condens. Matter Mater. Phys.* **1996**, *54* (16), 11169−11186.
(50) Kresse, G.; Furthmüller, J. Efficiency of *ab-initio* total energy calculations for metals and semiconductors using a plane-wave basis set. *Comput. Mater. Sci.* **1996**, *6* (1), 15−50.
(51) Blöchl, P. E. Projector augmented-wave method. *Phys. Rev. B: Condens. Matter Mater. Phys.* **1994**, *50* (24), 17953−17979.
(52) Perdew, J. P.; Burke, K.; Ernzerhof, M. Generalized gradient approximation made simple. *Phys. Rev. Lett.* **1996**, *77* (18), 3865−3868.
(53) Grimme, S.; Antony, J.; Ehrlich, S.; Krieg, H. A consistent and accurate *ab initio* parametrization of density functional dispersion correction (DFT-D) for the 94 elements H-Pu. *J. Chem. Phys.* **2010**, *132* (15), 154104.
(54) Grimme, S.; Ehrlich, S.; Goerigk, L. Effect of the damping function in dispersion corrected density functional theory. *J. Comput. Chem.* **2011**, *32* (7), 1456−1465.

https://dx.doi.org/10.1021/jacs.0c07051
J. Am. Chem. Soc. 2020, 142, 17499−17507